Gas Evolution Dynamics and Numerical Dissipation in Shock Capturing Schemes

Kun Xu*and Zuowu Li†

subject classification: *35L64, 76N10, 65M93, 76P05*
key words: *Riemann solver, flux vector splitting, flux difference splitting, shock instability*

submitted to Journal of Computational Physics, May 1999

*Corresponding author. Mathematics Department, The Hong Kong University of Science & Technology, Clear Water Bay, Kowloon, Hong Kong. Email:makxu@uxmail.ust.hk Fax:(852)2358-1643 Tel: (852)2358-7433

†Computational Fluid Dynamics Laboratory, Beijing University of Aeronautics and Astronautics, Beijing, China

Gas Evolution Dynamics and Numerical Dissipation in Shock Capturing Schemes

Abstract

This paper concerns the gas evolution dynamics in exact and approximate Riemann solvers, e.g. the Flux Vector Splitting (FVS) and the Godunov method. The dissipative mechanism in different gas evolution models will be analyzed. Many test cases are used to support the physical argument. The numerical examples include shock structure, laminar boundary layer, and 2D shock tube calculations. From the boundary layer case, the first order dissipative mechanism in the so-called second-order MUSCL-type FVS scheme is quantitatively evaluated. Also, the physical reason for shock instability in the Godunov method, i.e. carbuncle phenomena and odd-even decoupling, is presented.

1 Introduction

As pointed out by van Leer [13], a high resolution scheme usually consists of two parts, the reconstruction of the initial data and the dynamical evolution started from the constructed data. The reconstruction stage is a kinematic description of the flow variables. It tries to recover the continuous physical reality inside each cell from the discretized data. However, numerical dissipation is implicitly introduced in the reconstruction stage through the smearing of subcell structure and the amount of dissipation depends on the fluid velocity difference [18]. In this paper we are going to analyze the dissipative mechanism of shock capturing schemes in the gas evolution stage.

There are mainly two kinds of numerical flux functions derived from the inviscid Euler equations. The first group is the FVS schemes [11, 14], where the waves generated in the left and right hand side of a cell interface move across the cell boundary freely, and the flux has the form $F_{j+1/2} = F^+(W_j) + F^-(W_{j+1})$, where W_j and W_{j+1} are the left and right states. In the FVS scheme, a positive flux function from the left state $F^+(W_j)$ can move across the cell interface regardless of the existence of the right state W_{j+1}. In other words, there is no any dynamical interaction between the left and right states in the FVS scheme in the flux evaluation process. In the present paper, we are going to show that due to the free transport mechanism the artificial dissipation from the gas evolution stage in the FVS scheme is first order, and the viscosity coefficient is always proportional to the cell size, i.e. $\nu_{num} \sim \alpha \Delta x$. The linear relation between the viscosity coefficient and the cell size is even true for the second-order Muscl-type FVS scheme. This is also the basic reason for the robustness of the FVS scheme, such as the absence of numerical shock instability. However, this advantage also brings a disadvantage for the FVS scheme in solving the Navier-Stokes equations because the large numerical dissipation could easily poison the physical viscous term.

On the other hand, the Godunov method based on the exact Riemann solver accounts for the wave interactions in the gas evolution process [3]. Since the Godunov method is closely following the Euler solution in the gas evolution stage, if there is no projection dissipation introduced in the reconstruction stage, it can keep a precise shear layer in the 2D case once the shear layer is aligned with the mesh. Therefore, the gas evolution model in the Godunov method does not introduce any numerical dissipation. But, this advantage is associated with disadvantages in some cases, such as inability to stabilize a 2D shock front. Practically, any scheme which could capture a shock transition must have intrinsic dissipation. For the Godunov method, the dissipation is solely provided from the projection or the reconstruction stage. As a result, the artificial dissipation in the Godunov method depends not only on the flow distributions, but also on the mesh orientation, i.e. in which direction the Riemann solver is applied. Therefore, the form of the numerical dissipation in the Godunov method is basically inconsistent with the Navier-Stokes-type viscous term, and the Godunov method could possibly generate inappropriate solutions.

In this paper, we are going to use the Godunov and FVS schemes to solve the Navier-Stokes equations in both a shock structure and a laminar boundary layer. The reason for the different behavior of the FVS scheme in the shock and boundary layers is presented. Due to the same free transport mechanism between FVS and Kinetic FVS (KFVS) scheme, the inappropriate behavior of the Navier-Stokes KFVS scheme of Chou and Baganoff is also pointed out [1].

2 Numerical Observations

In this section, we are going to test the Godunov and van Leer FVS schemes in a few cases. In order to clearly distinguish the dynamics from the reconstruction and gas evolution stages, identical reconstruction method will be used for both schemes. In other words, any difference in the numerical behavior from these two schemes is purely from the different underlying gas evolution models.

2.1 Second-order Godunov and FVS Schemes

2.1.1 Reconstruction Stage

Following van Leer's Muscl idea, the numerical scheme is composed of an initial reconstruction stage followed by a dynamical evolution stage. At the beginning of each time step $t = 0$, cell averaged mass, momentum and energy densities are given. For a high order scheme, interpolation techniques must be used to capture the subcell structure. In the current paper, the van Leer limiter will be used to interpolate conservative variables directly.

Let $x_j = j\Delta x$ $(j = 0, 1, 2, ...)$ be a uniform mesh and Δx the mesh size. Let $x_{j+\frac{1}{2}} = (j + \frac{1}{2})\Delta x$ be the interface between cells j and $j + 1$. The cell averaged conservative variable is denoted by W_j, and its interpolated value in cell j is $\bar{W}_j(x)$, with two pointwise values $\bar{W}_j(x_{j-1/2})$ and $\bar{W}_j(x_{j+1/2})$ at the locations $x_{j-1/2}$ and $x_{j+1/2}$. To second order accuracy, the interpolated value in the j-th cell can be written as

$$\bar{W}_j(x) = W_j + L(W_{j-l}, ..., W_{j+l})(x - x_j) \quad \text{for} \quad x_{j-1/2} \le x \le x_{j+1/2},$$

where l is an integer and $2l + 1$ is the extent of the stencil. Here L is an interpolating function. For example, the second-order TVD interpolation has $l = 1$. The limiter we will use in the current study is the van Leer limiter

$$L(s_+, s_-) = S(s_+, s_-)\frac{|s_+||s_-|}{|s_+| + |s_-|},$$

where $S(u,v) = \text{sign}(u) + \text{sign}(v)$ is defined in terms of sign-functions, and $s_+ = (W_{j+1} - W_j)/\Delta x$ and $s_- = (W_j - W_{j-1})/\Delta x$ are the corresponding slopes for the conservative variables.

2.1.2 Gas Evolution Stage

In order to get a second order accuracy in time, we adapt the Muscl-Hancock approach [12]. Based on the interpolated data $\bar{W}_j(x)$ inside cell j, the values of $\bar{W}$ at two end points inside cell j are denoted as $W_j^L = \bar{W}_j(x_{j-1/2})$ and $W_j^R = \bar{W}_j(x_{j+1/2})$. Then, the interpolated boundary values W_j^L and W_j^R are evolved by a half time step $\frac{1}{2}\Delta t$ according to

$$\bar{W}_j^L = W_j^L + \frac{1}{2}\frac{\Delta t}{\Delta x}[F(W_j^L) - F(W_j^R)]$$

and

$$\bar{W}_j^R = W_j^R + \frac{1}{2}\frac{\Delta t}{\Delta x}[F(W_j^L) - F(W_j^R)].$$

Based on the new states

$$W_L = \bar{W}_j^R \qquad \text{and} \qquad W_R = \bar{W}_{j+1}^L$$

the exact Riemann problem is solved in the Godunov method, from which the numerical fluxes can be obtained

$$F_{j+1/2}^I = F(W_{j+1/2}(0)).$$

Here $W_{j+1/2}(0)$ denotes the value of $W_{j+1/2}(x/t)$ at $x/t = 0$, and I means the inviscid flux.

For the Navier-Stokes equations, we use a second-order central difference scheme to evaluate the viscous flux across a cell interface $F_{j+1/2}^V$. The update of the conservative variables inside each cell becomes

$$W_j^{n+1} = W_j^n + \frac{\Delta t}{\Delta x}(F_{j-1/2}^I + F_{j-1/2}^V - F_{j+1/2}^I - F_{j+1/2}^V).$$

For the van Leer FVS scheme, the only difference from the above Godunov method is the flux evaluation, where the flux vector splitting formulation is used [14].

2.2 Numerical Results

In this subsection, we are going to compare the results from the second-order Godunov and van Leer FVS scheme in three test cases. Also, Chou and Baganoff's NS KFVS scheme will be tested in the laminar boundary layer case.

2.2.1 Navier-Stokes Shock Structure

The first test case is the standard Sod test case [10]. However, instead of solving the inviscid Euler equations, we are going to solve the Navier-Stokes equations with unit Prandtl number directly, where the kinematic viscous coefficient ν used in this case is set to be a constant, i.e. $\nu = 0.0001$. The computational domain covers $x \in [0,1]$, and the total number of mesh points used here are $N = 50, 200, 400, ..., 100000$. The corresponding cell size becomes $\Delta x = 1/N$. Initially, with the coarse mesh, the physical viscous effect is much less than the intrinsic numerical dissipation from the reconstruction stage [18], and the artificial shock front is always composed of one or two grid points. Fig.(1) and (3) present the density distributions using

$100, 200, 400$, and 800 grid points from these two schemes. The fixed number of grid points in the numerical shock region means that the numerical dissipation introduced in the reconstruction stage is always proportional to the cell size once the shock layer of the viscous equations cannot be properly resolved by the cell size. From the above Figures, we can clearly observe the equivalence between these two schemes in the capturing of the numerical shock. With a mesh refinement, the reconstruction dissipation decreases with the increasing of resolution in the reconstructed data. As a result, the physical viscous term becomes important. As shown in Fig.(2) and (4), the shock structure emerges from these two schemes as mesh size goes down to $1/3200$ or even smaller. In these Figures, the solid line is the exact Navier-Stokes solution of the shock structure. With the mesh size $\Delta x = 1/6400$, the entropy density inside the shock layer is also captured accurately, as shown in Fig.(5). Again, the solid line is the exact solution. Fig.(5) shows that the entropy distribution is not a monotonic function across the shock layer. These phenomena also happen in inviscid Euler calculations when a numerical shock is across a few grid points [9]. So, the entropy equation has to be used carefully in the design of a monotonic numerical scheme.

For the shock structure calculation, both the Godunov and the FVS scheme can present accurate solutions. In other words, it is hard to distinguish the different gas evolution mechanism in these two schemes. It is partially due to the self steepening mechanism of the shock wave. A detail analysis will be presented in section 3. Since the KFVS and FVS have the same physical basis, it is not surprising that the Navier-Stokes KFVS scheme of Chou and Baganoff can also give an accurate shock structure calculation [1]. However, this test case alone cannot guarantee that FVS scheme is appropriate for the calculation of the Navier-Stokes solutions. Also, it should be mentioned that the implementation of Hancock method to get second order temporal accuracy is very important in the capturing of moving shock structure in both Godunov and FVS schemes; otherwise the shock structure appears steeper from a first order time accurate scheme. In other words, the first order time accuracy introduces negative dissipation in the gas evolution stage.

2.2.2 2D Laminar Boundary Layer

In the following, we are going to test these two schemes in a laminar boundary layer. Many shock capturing schemes have claimed to give accurate Navier-Stokes solutions, although some of them are dynamically similar to the FVS scheme. It is probably favorable to get a standard and reasonable test case in order to compare different schemes. In the following, we design such a test case for this purpose [16].

The computational domain used in this case is $[x]\times[y] = [1, 320]\times[1, 120]$ and the numerical mesh is orthogonal with 320×120 grid points in the $x - y$ plane. The cell sizes are $\Delta x = 1.0$ and $\Delta y = 1.0$. The flat plate is placed at the lower boundary ranging from $x = 80$ to $x = 320$ with total length $L = 240$. The inflow condition at $x = -\infty$ is

$$(\rho, U, V, p)|_{x=-\infty,y,t} = (1, 3, 0, \frac{9}{\gamma M^2}),$$

where M is the fixed Mach number with the value $M = 0.3$ and $\gamma = 1.4$. In this test case, the

Reynolds number is defined as

$$\mathrm{Re} = \frac{UL}{\nu_{phy}},$$

and the value of ν_{phy} is equal to 0.024 which gives $\mathrm{Re} = 30,000$. No-slip boundary condition is imposed on the flat plate by creating two "ghost cells" inside boundary which reverse the velocities of the two cells above the flat plate. The Euler boundary condition with x-direction velocity slip is used for the other part of the lower boundary. Appropriate nonreflecting boundary condition based on the one-dimensional Riemann invariants is used at the left and upper boundaries. For example, in the left boundary, Riemann invariants are

$$R_1 = U_{-\infty} + \frac{2C_{-\infty}}{\gamma - 1}$$

constructed from the state at $-\infty$, and

$$R_2 = U_1 - \frac{2C_1}{\gamma - 1}$$

obtained from the state at the first cell inside the computational domain, where U is the fluid velocity and C is the sound speed. From the above two relations, we can determine the velocity U_0 and the sound speed C_0 in the first cell outside the left boundary. Also, with the help of entropy invariant condition,

$$\frac{p_{-\infty}}{\rho_{-\infty}^{\gamma}} = \frac{p_0}{\rho_0^{\gamma}},$$

we can determine other conservative variables at the cell 0. Then, the flow variables in the cell -1 are set to be equal to the corresponding values at the cell 0. Simple extrapolation of the conservative variables are used at the right boundary.

The output velocities are defined as

$$u = \frac{U}{U_\infty} \qquad , \qquad v = \frac{V}{U_\infty}\sqrt{\frac{U_\infty(x - x_s)}{\nu_{phy}}},$$

where $x_s = 79.5$ is the location of the leading edge of the flat plate. The numerical results are plotted at the locations $x = 150, 200$, and 250, and the distance y in the y-direction above the flat plate is normalized by

$$\eta = y\sqrt{\frac{U_\infty}{\nu_{phy}(x - x_s)}}.$$

Fig.(6) and (7) show the u and v velocity distributions calculated by the Godunov and van Leer FVS schemes. The solid lines are the exact Blasius solution. As shown in these figures, the Godunov method can give accurate laminar boundary solution, while the FVS scheme can hardly capture the shear layer correctly. In the v velocity distribution, the Godunov scheme gives a velocity jump in the first cell above the flat plate. The reason for this is still under investigation.

Both u and v velocities are much smeared in the van Leer FVS scheme. Since we have used the same reconstruction technique for the preparation of the initial data, the different behaviors between the Godunov and FVS methods must come from the gas evolution model, i.e. the dissipative mechanism underlying the flux evaluation. A detail analysis will be presented in section 3.

Recently, Chou and Baganoff proposed a Navier-Stokes KFVS Scheme [1]. In their case, they tested the shock layer and showed that their NS KFVS scheme gives an accurate solution. However, applying the Chou-Baganoff scheme to the boundary layer problem, we find that their scheme behaves basically in the same way as the van Leer FVS scheme. The u and v velocities are shown in Fig.(8).

2.2.3 Odd-even Decoupling Case

Quirk [7] catalogued a few cases, which could trigger the failure of upwinding schemes, especially the Roe's method [8]. Some of the failures are due to the linearization of the Euler equations, such as negative density and expansion shocks, and others are due to intrinsic properties of the Godunov method. In the following we test both the 2nd-order Godunov and FVS schemes in the odd-even decoupling case [7]. This test is about a normal shock propagating in the 2D shock tube, where the location of central line is perturbed odd-evenly with a magnitude of 10^{-6}. As shown in [7], any small fluctuation gets amplified quickly in the Roe scheme, and the initial shock front is totally destroyed after the shock passes through some distance in the shock tube. Similar phenomena happens to the Osher's scheme.

Fig.(9a) shows the result from the 2nd-order Godunov method by solving the inviscid Euler equations, and Fig.(9b-d) are the results of the Navier-Stokes equations. Fig.(9e) presents the result from the FVS scheme with $\nu_{phy} = 0.0$. From these figures, we can clearly observe that the Godunov method will amplify the initial small perturbations and generate instability after the shock. However, the instability can be effectively removed by solving the viscous equations. For the FVS scheme, the density distribution in the whole domian is extremely smooth and the perturbation is effectively suppressed. This test case clearly shows the robustness of the FVS scheme.

With the help of above three test cases in this section, we are going to analyze the dissipative mechanism in both FVS and the Godunov methods in the next few sections.

3 Dissipative Mechanism in FVS Scheme

3.1 Numerical Dissipation

Similar to the KFVS scheme [16], all FVS schemes have particles or waves free transport mechanism. As a result, the FVS scheme makes the particle mean free path $\bar{l}$ be equal to the cell size Δx. Since the viscosity coefficient $\bar{\nu}$ is proportional to the mean free path, i.e. $\bar{\nu} \sim \bar{c}\bar{l}$, where $\bar{c}$ is the local sound speed, the artificial viscosity $\bar{\nu}$ in the FVS scheme must be proportional to the cell size Δx, i.e. $\nu_{num} = \alpha \Delta y$ in the boundary layer case. In the Appendix, the detail derivation of the viscosity coefficient of the FVS scheme is presented.

In order to verify the above analysis, we have done a mesh refinement study in the boundary layer case for the FVS scheme. The artificial viscosity coefficient ν_{num} is obtained by fitting the Blasius solution with the numerical u-velocity distribution at the location of $x = 200$.

Table 1. The Viscosity vs. Cell Size, where $\nu_{phy} = 0.024$

Δy	1	2/3	1/2	1/3	1/4
$\sqrt{\nu_{total}/\nu_{phy}}$	2.1	1.65	1.4	1.2	1.12
$\sqrt{\nu_{num}/\nu_{phys}}$	1.9	1.45	1.17	0.86	

In Table 1, we list the experimental data containing cell size Δy and the viscousity coefficient. Here ν_{total} is obtained from the total viscous effect when the FVS scheme is used to solve the Navier-Stokes equations with $\nu_{phy} = 0.024$. Fig.(10) shows the fitting process to get the above viscosity coefficients. If we remove the physical viscous term ν_{phy} and solve the "Euler equations" directly using the FVS scheme in the boundary layer, we can also fit the boundary layer solution to get the purely numerical viscous coefficient ν_{num}. Fig.(11) shows this fitting process, from which the relationship between $\sqrt{\nu_{num}/\nu_{phy}}$ and Δy can be obtained. As shown in Fig.(11), at $\Delta y = 1/3$, the numerical viscosity becomes smaller than ν_{phy} and the boundary layer thickness is thinner. In Fig.(12), we plot the data in Table 1 and clearly observe the linear dependence between cell size Δy and numerical viscous coefficient ν_{num}. So, we have the relation $\nu_{num} \sim \alpha\Delta y$ based on the numerical results from the FVS scheme and this property is independent of the spatial order in the reconstruction stage. From the numerical data in Table 1, we can get $\alpha \sim 0.11$. This number is on the same order as the theoretical analysis in the Appendix.

From the above analysis, we can understand that the development of a second-order FVS scheme for the Navier-Stokes equations is impossible. The free transport mechanism underlying all FVS schemes generate first-order dissipation. This is the basic reason for the robustness of the FVS scheme, such as the avoiding the carbuncle phenomena and odd-even decoupling, see Fig.(9e). Furthermore, as analyzed in [16], the parameter α in $\nu_{num} = \alpha\Delta x$ should be proportional to the pressure. Since the pressure decreases from the leading part to the rear part of the flat plate, the numerical viscosity is not constant, and α decreases along the direction from 150 to 250. This observation is consistent with the numerical results in Fig.(7). At different locations, the numerical solutions cannot collapse to the same curve, and ν_{num} is decreasing from the locations $x = 150$ to 250.

For the Naver-Stokes solutions, adaptive mesh is usually used in the boundary layer, where the mesh size is very small close to the boundary and become large away from the boundary. If the FVS scheme is used here, due to the difference in the mesh size, the dissipation coefficient ν_{num} will be different at different locations in the y-direction. As a result, the similarity solution will be lost, such as Fig.10(a) in [2], where it is impossible to fit the rounded corner by modifying the viscosity coefficient in the Blasius solution. In our case, since we are using a uniform mesh, the numerical viscosity coefficient is basically a constant in each x location. Therefore, the similarity solution from FVS scheme can be basically kept.

The physical analysis based on KFVS scheme in [17] and the above numerical observation about FVS scheme are consistent. After understanding the dissipative mechanism in the FVS schemes, we can conclude that it is difficult to get an accurate Navier-Stokes solution using FVS scheme if the mesh size is not small enough. The intrinsic weakness of the FVS method should appear in all schemes, where the methodology $F = F^+ + F^-$ is used to construct fluxes.

3.2 Different Behavior of FVS Scheme at Shock and Boundary Layers

The FVS scheme behaves differently in the shock and boundary layer calculations. The basic reason is the following.

Suppose we need $N \sim 10$ cells to resolve the physical shock front and boundary layer. Then, the shock thickness l_s can be expressed as

$$l_s \sim \frac{\nu^s_{phy}}{\Delta U} \sim N\Delta x,$$

where s means shock case, and the boundary layer thickness l_b is

$$l_b \sim \sqrt{\frac{\nu^b_{phy} L}{\Delta U}} \sim N\Delta x,$$

where b means boundary. In both cases, phy refers to the physical viscosity. In the boundary layer case, ΔU is the velocity jump from the flat plate $U = 0$ to the velocity U_∞ at far upstream, and L is the length of the flat plate. Note that the velocity jump in both shock and boundary cases can be considered on the same order as the test cases presented in the last section. From the above equations, the physical viscosity in the shock and boundary layer become

$$\nu^s_{phy} \sim N\Delta x \Delta U \qquad , \qquad \nu^b_{phy} \sim \frac{(N\Delta x)^2 \Delta U}{L}.$$

Suppose that we use the FVS scheme to simulate shock and boundary layers. Because the numerical dissipation coefficient in the FVS scheme is proportional to the cell size, i.e. $\nu_{num} \sim \alpha\Delta x$, the ratio between the numerical and physical viscosity coefficients are

$$\frac{\nu_{num}}{\nu_{phy}}|_{shock} \sim \frac{\alpha}{N\Delta U} \tag{3.1}$$

in the shock region, and

$$\frac{\nu_{num}}{\nu_{phy}}|_{boundary} \sim \frac{\alpha L}{N^2 \Delta x \Delta U},$$

in the boundary layer case. Since $L \sim N^2 \Delta x$ in our boundary layer test case, the above relation goes to

$$\frac{\nu_{num}}{\nu_{phy}}|_{boundary} \sim \frac{\alpha}{\Delta U}. \tag{3.2}$$

Comparing Eq.(3.1) and (3.2), from the same amount of numerical dissipation, the artificial viscosity plays a much more important role in the boundary layer than that in the shock layer once both layers are resolved by certain number of points, such as $N \sim 10$.

4 Dissipative Mechanism in the Godunov Gas Evolution Model

The Godunov method is based on the exact Euler solution, the so-called Riemann problem in the gas evolution stage. Therefore, the numerical dissipation provided in the Godunov method must come from the projection and reconstruction stage. The lack of numerical dissipation in the gas evolution stage has advantage and disadvantage. In this section, we are going to analyze the Godunov gas evolution model and present an explanation for the shock instability.

4.1 Exact Riemann Solver

The Riemann problem is defined as an initial value problem for the Euler equations. In the 1-D case, with the following initial condition at $t = 0$,

$$(\rho, U, p) = \begin{cases} (\rho_L, U_L, p_L), & x \le 0, \\ (\rho_R, U_R, p_R), & x > 0, \end{cases} \tag{4.3}$$

the entropy-satisfying solutions are the following: the left state (ρ_L, U_L, p_L) is connected to the right state (ρ_R, U_R, p_R) by a 1-shock or 1-rarefaction wave, a 2-contact discontinuity, and a 3-shock or a 3-rarefaction wave. The 2-contact discontinuity separates two constant states (ρ_I, U^*, p^*) and (ρ_{II}, U^*, p^*), so that (U, p) are continuous across the contact discontinuity. For example, in Fig.(13), the 1-wave is a rarefaction and the 3-wave a shock. There is standard technique to obtain the solutions around a contact discontinuity [12]. Basically, the Godunov method is closely following the solution of the inviscid Euler equations.

Once the solution of the Riemann problem is obtained, the flow variables at $x = 0$, i.e. (ρ_I, U^*, p^*) in Fig.(13), are used to construct fluxes. The Godunov method uses these fluxes across each cell interface to update the flow variables. In order to understand the gas evolution model in the Godunov method, we have to understand the underlying assumption in the process of evaluating the fluxes. For the Euler equations, the corresponding fluxes are obviously

$$\begin{pmatrix} F_\rho \\ F_{\rho U} \\ F_{\rho\epsilon} \end{pmatrix} = \begin{pmatrix} \rho U \\ \rho U^2 + p \\ \frac{1}{2}\rho U^3 + \frac{\gamma}{\gamma-1} pU \end{pmatrix}. \tag{4.4}$$

For example, in Fig.(13), the fluxes at $x = 0$ can be written as $(\rho_I U^*, \rho_I U^{*2} + p^*, \frac{1}{2}\rho_I U^{*3} + \frac{\gamma}{\gamma-1} p^* U^*)^T$. From the flow variables (ρ, U, p) to the above flux functions $(F_\rho, F_{\rho U}, F_{\rho\epsilon})$, it is implicitly assumed that the gas is staying in an equilibrium state. In other words, whatever the real flow situations is, the state (ρ_I, U^*, p^*) at the cell interface always corresponds to the equilibrium state in the Godunov method, even for the fluid inside a numerical shock layer, see Fig.(14).

As we know, the intermediate points in the numerical shock region have to be regarded as points inside a shock structure, where flow particles stay in a nonequilibrium state and a dissipative mechanism is crucially important to translate kinetic energy into thermal energy and make the shock transition smooth. But, the gas evolution model of the Godunov method inappropriately assigns the equilibrium state there at the cell interface. Ignoring dissipation in the gas evolution stage in the discontinuous region is one of the flaws of the Godunov method. Fortunately, as analyzed in [18], the projection stage can provide a certain amount of dissipation in the shock region to capture numerical discontinuities. However, in the slowly moving shock case, the projection dissipation alone is not enough to construct a smooth shock transition, and oscillations always appear after the shock. If the viscous governing equations are solved, keeping a certain amount of dissipation in the gas evolution stage can effectively remove post-shock oscillations. See Fig.(15).

4.2 Shock Instability in the Godunov Method

4.2.1 Projection Dissipation In 2D Case

In the 2-D case, for any flow distribution with velocity $(\mathbf{U_1}(x,y), \mathbf{U_2}(x,y))$ and density $(\rho_1(x,y), \rho_2(x,y))$ in a small volume, the dissipation provided in the projection stage is

$$\Delta E_k = E_k - \bar{E}_k, \tag{4.5}$$

where E_k is the total kinetic energy before the averaging and $\bar{E}_k$ is the kinetic energy after the averaging. The difference in the kinetic energy before and after averaging is translated into the thermal one. For simplicity, the volumes occupied by $(\rho_1, \mathbf{U_1})$ and $(\rho_2, \mathbf{U_2})$ are assumed to be the same and equal to $1/2$. From the conservations of the mass and momentum, we have

$$\bar{\rho} = \frac{1}{2}(\rho_1 + \rho_2)$$

and

$$\bar{\rho}\bar{\mathbf{U}} = \frac{1}{2}(\rho_1 \mathbf{U_1} + \rho_2 \mathbf{U_2}).$$

As a result, the kinetic energy before the averaging is

$$E_k = \frac{1}{4}(\rho_1 \mathbf{U_1}^2 + \rho_2 \mathbf{U_2}^2),$$

and after the averaging

$$\bar{E}_k = \frac{1}{2}\bar{\rho}\bar{\mathbf{U}}^2.$$

With the above relations, the difference in the kinetic energy can be obtained,

$$\Delta E_k = \frac{1}{4}\frac{\rho_1\rho_2}{\rho_1 + \rho_2}(\mathbf{U_1} - \mathbf{U_2})^2_{\hat{n}},$$

where $\hat{n}$ is the direction from which the fluid velocity distributions are $\mathbf{U_1}, \mathbf{U_2}$. So, the projection stage in the Godunov method provides the following dissipation

$$\text{dissipation} \sim \frac{\rho_1\rho_2}{\rho_1\rho_2}(\mathbf{U_1} - \mathbf{U_2})^2_{\hat{n}}. \tag{4.6}$$

Again, $\hat{n}$ is the direction in which the Riemann solution is evaluated. For a 1-D flow, $(\mathbf{U_1} - \mathbf{U_2})$ is on the same direction as $\hat{n}$ and the dissipation is always proportional to $(U_1 - U_2)^2$. Therefore, in the 1-D case, the velocity difference provides intrinsic dissipation to the Godunov method in the shock region. However, in the 2-D case, the velocity difference between $\mathbf{U_1}$ and $\mathbf{U_2}$ depends on which direction you look at the flow, and the dissipation in the Godunov method becomes mesh-oriented. As shown in Fig.(16), for the same fluid distribution in the 2-D case, i.e. a normal shock in the $\hat{x}$-direction, the velocity distribution $(\mathbf{U_1} - \mathbf{U_2})_{\hat{n}}$ is different when viewed from different directions $\hat{n}$. So, the dissipative term in Eq.(4.6) becomes directionally dependent. As shown in the case (b) of Fig.(16), for a 2-D normal shock in the $\hat{x}$-direction, the dissipation provided in the $\hat{y}$-direction becomes $(\mathbf{U_1} - \mathbf{U_2})_{\hat{y}} \sim 0$, because $\mathbf{U_1}$ and $\mathbf{U_2}$ appear as parallel flows with the same velocity magnitude in that direction.

4.2.2 Shock Instability

The documented observations of the shock instability are scattered in many papers. The influential paper by Quirk for the first time systematically presented the observation and analysis [7]. After that, the explanation of this numerical shock behavior has attracted much attention. A short list of references includes [4, 5, 6], and references therein.

In order to have shock instability, such as the carbuncle phenomena or odd-even decoupling, the numerical fluid has to satisfy the following condition [7, 5]:

Shock propagates and is aligned with the mesh.

From the above condition, if the shock front is aligned with the mesh, the projection dissipation (4.6) can be provided only in the direction normal to the shock front, such as in the x-direction. There is almost no projection dissipation provided in the direction along the shock front due to the equal velocities.

Now suppose that a stationary shock is staying in the $\hat{x}$-direction. Inside the shock layer, due to numerical perturbations, it is possible that a fluid element will move from cross section S_A to S_B through the streamline converging or diverging, such as that shown in Fig.(17). For this element, the momentum conservation gives

$$pS_A + \rho U^2 S_A + pdS_A = (p+dp)(S_A+dS_A) + (\rho + d\rho)(U+dU)^2(S_A+dS_A). \tag{4.7}$$

The continuity equation is $d(\rho U S_A) = 0$, or

$$\rho U dS_A + \rho S_A dU + S_A U d\rho = 0.$$

Multiplying the above equation by U and subtracting it from Eq.(4.7), we have

$$dp = -\rho U dU,$$

which means that the pressure change is always out of phase with the velocity change. From aerodynamic theory for a quasi-one-dimensional flow, we have

Case(1). For $0 \le M \le 1$ (downstream side), an increase in velocity (positive dU) is associated with a decrease in area (S_A), and vice versa. Therefore, the velocity increases (pressure decreases) in a converging streamline case and decreases (pressure increases) in a diverging streamline case.

Case(2). For $M > 1$ (upstream side), the velocity increases (pressure decreases) in diverging streamline case and decreases (pressure increases) in the converging streamline case.

On the subsonic side, once there is perturbation inside the numerical shock front, an increase of velocity is associated with a decrease of pressure in the converging streamline case, see Fig.(18). Physically, the shear viscosity will strongly take effect to reduce the velocity differences and stabilize the numerical shock structure. However, following the inviscid Euler solution in the y-direction (no projection dissipation provided in this direction) will give a different answer. The exact 1-D Riemann solver in the y-direction does not recognize the x-component velocity differences due to the inviscid nature. The only dynamical influence involved in the Riemann solver in this direction is the pressure difference. Since the fluid in the surrounding cells has a higher pressure, it will move toward the center. As a consequence, the fluid in the central cells passes through an even narrower cross section, and the fluid speed gets even higher due to the converging of streamlines. Therefore, the pressure in the central cells becomes even lower. So, the use of the exact Riemann solver in the y-direction could only help to amplify the initial perturbation, and the instability will be formed in the subsonic region, where $M < 1$.

On the supersonic side of the shock layer, such as on the right hand side of Fig.(17), in the streamline converging case, an increase in velocity will be associated with an increase in pressure. So, the central high pressure gas will expand and stop the converging of the streamlines. Therefore, in the upstream side $M > 1$, the structure is theoretically stable to small perturbations.

Fig.(19) shows the density distributions in Fig.(9a) along the x-direction at different y locations. Fig.(19) clearly shows that the density fluctuation gets amplified on the downstream side, i.e. $M < 1$. The numerical observation is consistent with the above analysis.

The above analysis of the Godunov dissipative mechanism also validates the following numerical observation. If the shock front is not precisely aligned with the mesh, the projection dissipation will exist in both directions. For example, when the shock front in Fig.(9) is titled by 10 degree, the new density distribution in the shock tube is shown in Fig.(20), where the projection dissipation takes effect in both directions to eliminate the shock instability.

Liou [5] pointed out that in order to have shock instability the mass flux due to a pressure difference is not zero, such as $D^{(p)} \neq 0$ in the dissipative term $\mathcal{D} = \mathcal{D}^{(\rho)}\Delta\rho + \mathcal{D}^{(U)}\Delta U + \mathcal{D}^{(p)}\Delta p$ of the full flux function $F_{j+1/2} = \frac{1}{2}(F_j + F_{j+1}) + \mathcal{D}$. The analysis in this section validates Liou's conjecture that $\mathcal{D}^{(p)} \neq 0$ is accompanied by an instability. If $\mathcal{D}^{(p)} = 0$, the initial pressure difference in the y-direction will not push the fluid toward the central cells, and no instability will be formed. Unfortunately, even for the exact Riemann solver, $\mathcal{D}^{(p)} \neq 0$ always holds. So, shock instability is intrinsically rooted in the Godunov method if the inviscid Euler equations are considered as the governing equations in the numerical shock region in the $\hat{y}$-direction. On the other hand, if the viscous equations are solved in the gas evolution stage, the instability can be properly removed, such as these cases shown in Fig.(9). So, in some sense, it tells us that we have to solve the viscous governing equations in the discontinuous shock region, and follow the physical reality there in order to remove all pathological behavior.

For the shock instability case, Quirk used a saw-tooth initial condition to test the response from the Roe's Riemann solver [7]. It was observed that the initial density perturbation goes to $\hat{\rho}^{\infty} = \hat{\rho}^0/\tilde{a}^2$, where $\tilde{a}$ is the local sound speed. At the same time, the pressure perturbation decays. Similar analysis was also given in [6]. In these analysis, in order to get the shock instability, as pointed out by Quirk [7], *a systematic* pressure perturbation is needed to amplify $\hat{\rho}^{\infty}$. Then, the question is where the systematic perturbation comes from. Actually, Quirk's analysis is only based on the solution of an initially saw-tooth shear layer, it totally ignores the basic fact that instability happens around the numerical shock, where the $\hat{x}$-direction fluid velocities change dramatically across the shock layer.

5 Conclusion

In this paper, we test the Godunov and FVS schemes in the shock structure, boundary layer, and 2D shock tube cases. All numerical observations are consistent with the physical analysis.

From this paper, we understand that numerical dissipation coefficient in the FVS scheme is always proportional to the cell size, which is due to the particle or wave free transport mechanism. Therefore, the numerical dissipation in FVS schemes is too large to give an accurate Navier-Stokes solution. It is also shown that the Navier-Stokes KFVS scheme of Chou-Baganoff cannot give correct Navier-Stokes solutions either. The reason for the different behaviors of the FVS scheme in the shock and boundary layers is pointed out.

On the other hand, the Godunov method gives accurate results in both unsteady shock structure and boundary layer calculations. However, since numerical dissipation in the Godunov method comes from the projection and reconstruction stages, dissipation is tightly related to the mesh orientation. The absence of dissipation in the gas evolution model of the Godunov method amplifies the post-shock oscillations and shock instability.

In order to develop more accurate and robust numerical schemes for the compressible flow simulation, we have to consider the viscous governing equations directly in the discontinuity region. No perfect scheme, or the Riemann solver, will be obtained if only the Euler equations are regarded as the governing equations.

Appendix: The Numerical Viscous Effect in the van Leer FVS Scheme

For two adjacent cells inside the boundary in the y-direction, the flow distribution can be described by the following figure.

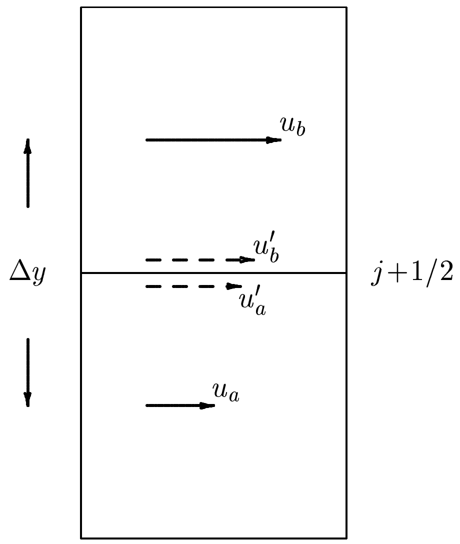

Since we are going to analyze a second-order scheme, from the x-direction velocities u_a and u_b and the corresponding values in surrounding cells, the van Leer limiter will give u'_a and u'_b as the interpolated velocities at the cell interface $j+1/2$. Due to the x-velocity differences in u'_a and u'_b, the van Leer splitting function gives a net flux of x-momentum across the cell interface, which is the numerical shear stress,

$$\tau = \frac{1}{4}\rho c(u'_b - u'_a), \tag{5.8}$$

where c is the sound speed. At the same time, according to the shear stress definition, we have

$$\tau = \rho\nu \frac{du}{dy}, \tag{5.9}$$

and du/dy can be formally defined as

$$\frac{du}{dy} = \frac{u_b - u_a}{\Delta y}.$$

From Eq.(5.8) and (5.9), we get the following kinematic viscosity coefficient ν in the 2nd-order van Leer FVS scheme,

$$\nu = \frac{1}{4} c \frac{u'_b - u'_a}{u_b - u_a} \Delta y. \tag{5.10}$$

The above linear relation between ν and cell size is consistent with the numerical observation in section 2. For the 1st-order FVS scheme, the numerical viscosity coefficient is

$$\nu = \frac{1}{4} c \Delta y.$$

Now let's apply Eq.(5.10) to the Blasius boundary layer solution. First. let's take a few points in the boundary layer, such as

η	0.4	1.2	2.0	2.8
u	0.13277	0.39378	0.62977	0.81152

From the above data, we have $u_a = 0.39378$ and $u_b = 0.62977$. Then, using the van Leer limiter, we can get $u'_a = 0.5177$ and $u'_b = 0.5271$. In the laminar boundary case in section 2, we have the pressure $p = 9/(\gamma M^2) = 71.4$ and the sound speed $c = \sqrt{\gamma p/\rho} = 9.997$. Therefore, the numerical viscosity coefficient becomes

$$\nu = \frac{1}{4} c \frac{u'_b - u'_a}{u_b - u_a} \Delta y = 0.099 \Delta y,$$

which is on the same order as the numerical observation, i.e. $\nu_{num} = 0.11\Delta y$.

The above analysis is based on a simplied physical model of the FVS scheme. We have ignored the Hancock method for time accuracy and the small v velocity inside the boundary layer. Also, there is some uncertainty in the selecting of points in the boundary layer. Even with the above approximations, the theoretical result is basically consistent with the numerical observation. For the 1st-order FVS scheme, the numerical viscosity coefficient becomes $\nu = 2.449\Delta y$, which is much larger than that in Eq.(5.10) of the "second-order" scheme.

Acknowledgments

Support was provided by Hong Kong Research Grant Council through RGC97/98.HKUST6166/97P.

References

[1] S.Y. Chou and D. Baganoff, *Kinetic Flux-Vector Splitting for the Navier-Stokes Equations*, J. Comput. Phys., **130** (1997), pp. 217-230.

[2] D. Drikakis and S. Tsangaris, *On the Solution of the Compressible Navier-Stokes Equations using Improved Flux Vector Splitting Methods*, Appl. Math. Modelling, **17** (1993), pp. 282-297.

[3] S.K. Godunov, *A Difference Scheme for Numerical Computation of Discontinuous Solutions of Hydrodynamic Equations*, Math. Sbornik, **47** (1959), pp. 271.

[4] J. Gressier and J.M. Moschetta, *On the Pathological Behavior of Upwind Schemes*, AIAA 98-0110 (1998).

[5] M.S. Liou, *Probing Numerical Fluxes, Positivity, and Entropy-satisfying Property*, AIAA 97-2035 (1997).

[6] M. Pandolfi and D. D'Ambrosio, *Upwind Methods and Carbuncle Phenomenon*, Computational Fluid Dynamics 98, **1** (1998), pp. 126-131, 4th ECCOMAS, Athens.

[7] J. Quirk, *A Contribution to the Great Riemann Solver Debate*, Int. J. Num. Met. in Fluids, **18** (1994), no.6.

[8] P.L. Roe, *Approximate Riemann Solvers, Parameter Vectors and Difference Schemes*, J. Comput. Phys., **43** (1981), pp. 357.

[9] M.D. Salas and A. Iollo, *Entropy Jump Across an Inviscid Shock Wave*, ICASE Report 95-12 (1995).

[10] G. Sod, *A Survey of Several Finite Difference Methods for Systems of Nonlinear Hyperbolic Conservation Laws*, J. Comput. Phys., **27** (1978), pp. 1-31.

[11] J. L. Steger and R. F. Warming, *Flux vector splitting of the inviscid gas-dynamic equations with applications to finite difference methods*, J. Comput. Phys., **40** (1981), pp. 263-293.

[12] E. Toro, *Riemann Solvers and Numerical Methods for Fluid Dynamics*, Springer (1997).

[13] J. B. van Leer, *Towards the Ultimate Conservative Difference Scheme IV, A New Approach to Numerical Convection*, J. Comput. Phys., **23** (1977), pp. 276-299.

[14] B. van. Leer, *Flux-Vector Splitting for the Euler Equations*, ICASE report, NO.82-30 (1982).

[15] B. van. Leer, J.L. Thomas, P.L. Roe, R.W. Newsome, *A Comparison of Numerical Flux Formulas for the Euler and Navier-Stokes Equations*, AIAA paper 87-1104 (1987).

[16] K. Xu, *Gas-Kinetic Schemes for Unsteady Compressible Flow Simulations*, VKI for Fluid Dynamics Lecture Series 1998-03 (1998), Computational Fluid Dynamics.

[17] K. Xu, *Gas Evolution Dynamics in Godunov-type Schemes and Analysis of Numerical Shock Instability*, ICASE Report 99-6, NASA Langley Research Center.

[18] K. Xu and J. Hu, *Projection Dynamics in Godunov-type Schemes*, J. Comput. Phys., **142** (1998), pp. 412-427.

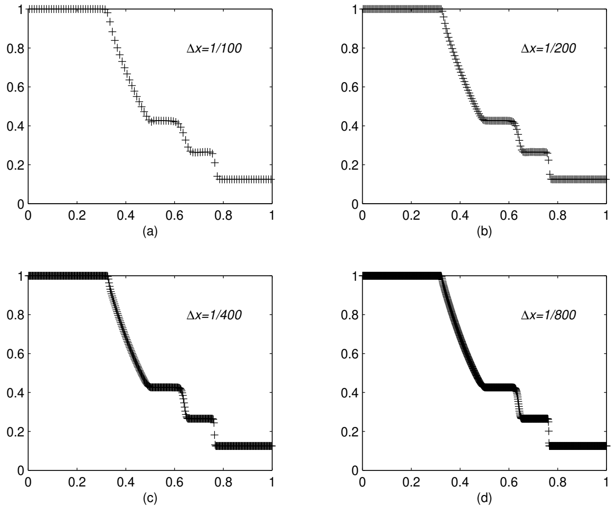

Figure 1: Density distribution in Sod test case using 2nd-order NS Godunov method for the Navier-Stokes Equations with $\nu_{phy} = 0.0001$. The figures (a)-(d) represent the results obtained using different cell size.

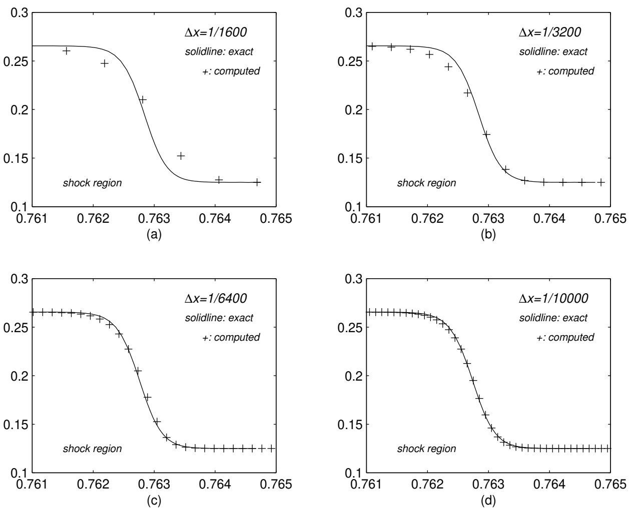

Figure 2: Density distribution in the shock region using 2nd-order NS Godunov method for the Navier-Stokes Equations. The solid line is the exact solution.

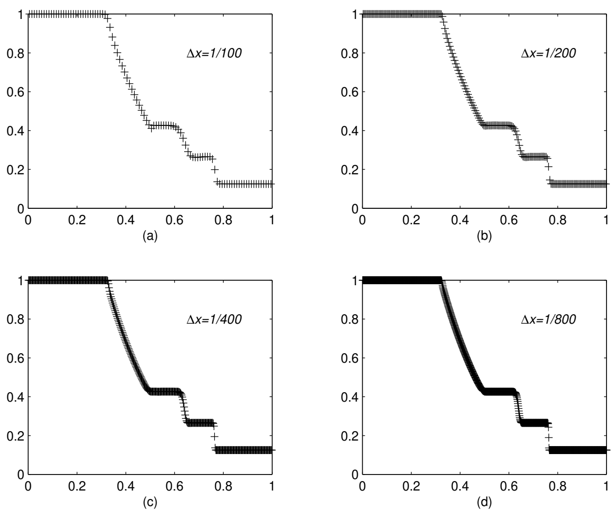

Figure 3: Density distribution in Sod test case using 2nd-order NS van Leer FVS method for the Navier-Stokes Equations with $\nu_{phy} = 0.0001$. The figures (a)-(d) represent the results obtained using different cell size.

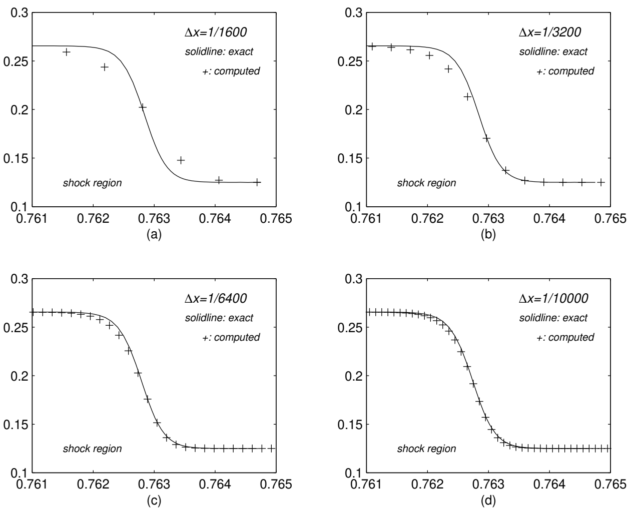

Figure 4: Density distribution in the shock region using 2nd-order NS van Leer FVS method for the Navier-Stokes Equations. The solid line is the exact solution.

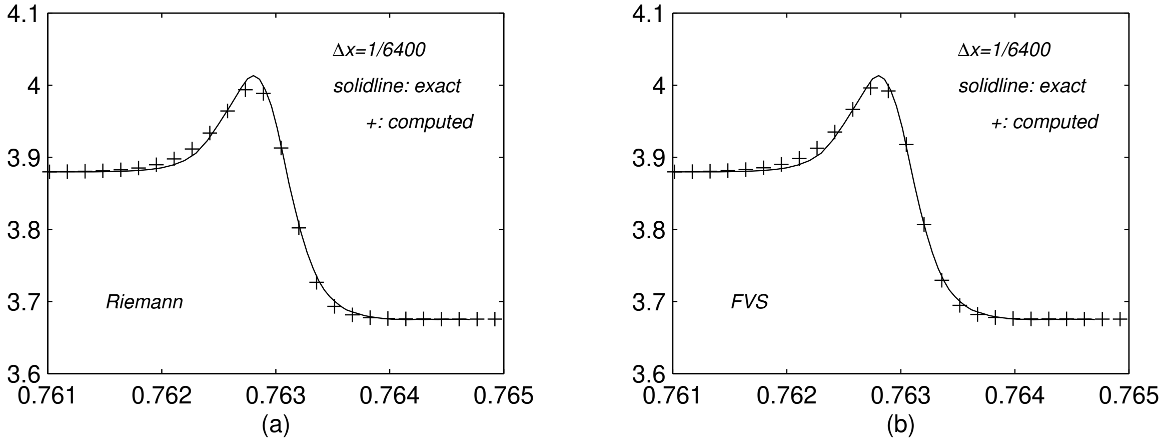

Figure 5: Entropy (p/ρ^{γ}) distribution across the shock layer. (a): 2nd-order NS Godunov method, (b): 2nd-order NS FVS scheme.

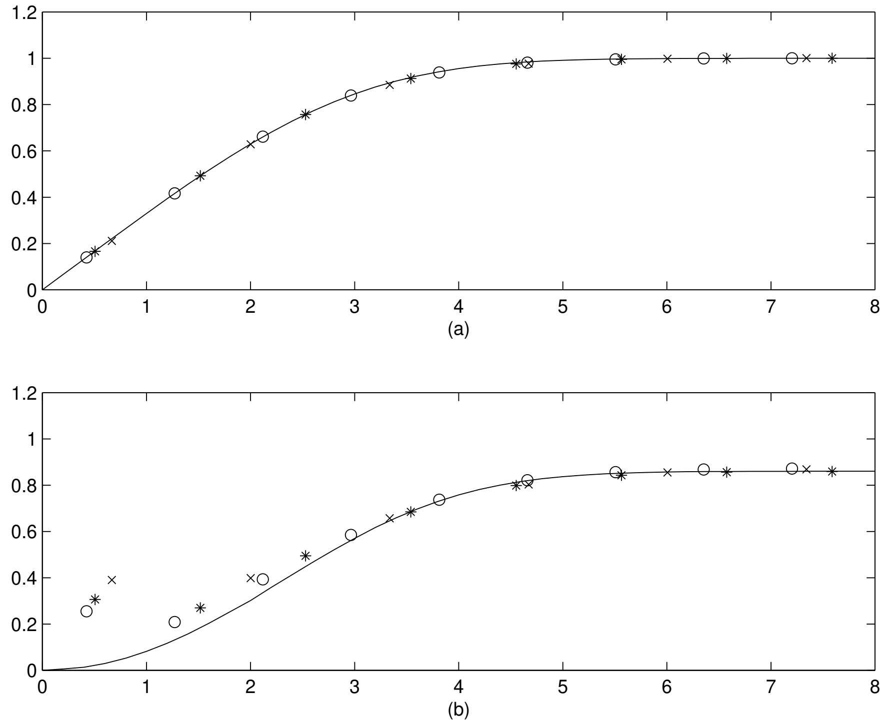

Figure 6: 2nd-order NS Godunov method. (a): u velocity distribution vs. η, (b): v velocity distribution vs. η. The output locations are: $\times$: $x = 150$, $*$: $x = 200$, $\circ$: $x = 250$. The solid line is the exact solution.

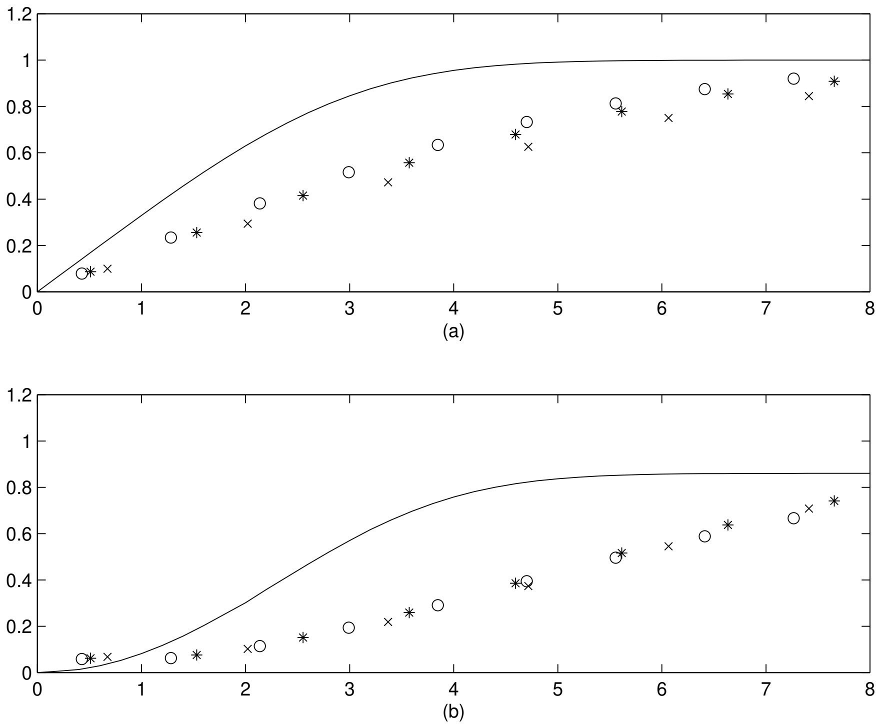

Figure 7: 2nd-order NS van Leer FVS scheme. (a): u velocity, (b): v velocity distribution. The output locations are: $\times$: $x = 150$, $*$: $x = 200$, $\circ$: $x = 250$. The solid line is the exact Blasius solution. From Fig.(a), we know that $\circ$ corresponds to the least numerical dissipation, then $*$ and $\times$.

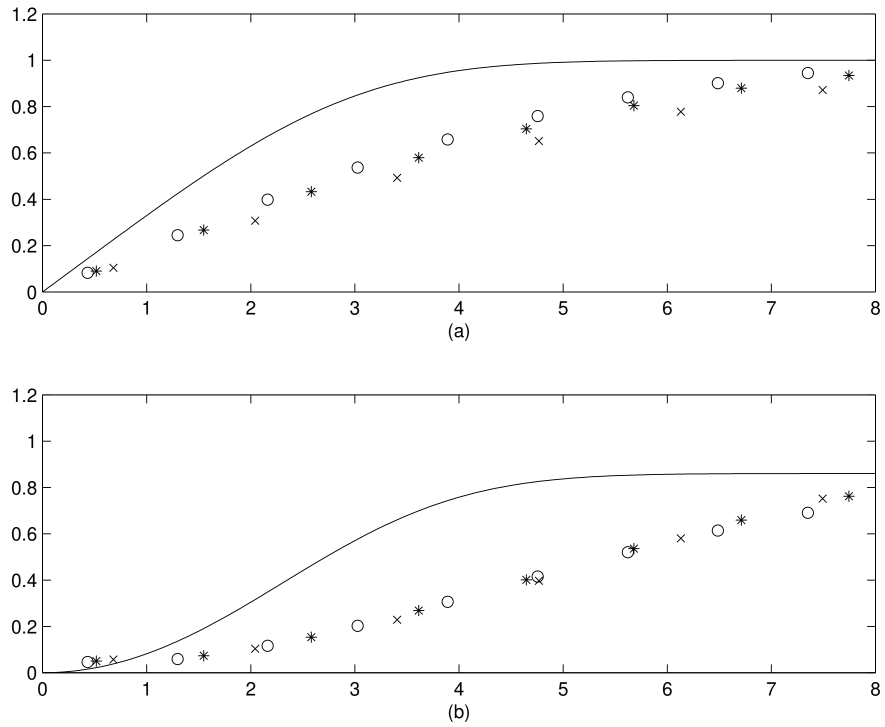

Figure 8: Chou-Baganoff NS KFVS Scheme for the Boundary layer solution [1]. (a): u velocity distribution vs. η, (b): v velocity distribution vs. η. The output locations are: $\times$: $x = 150$, $*$: $x = 200$, $\circ$: $x = 250$. The solid line is the exact Blasius solution.

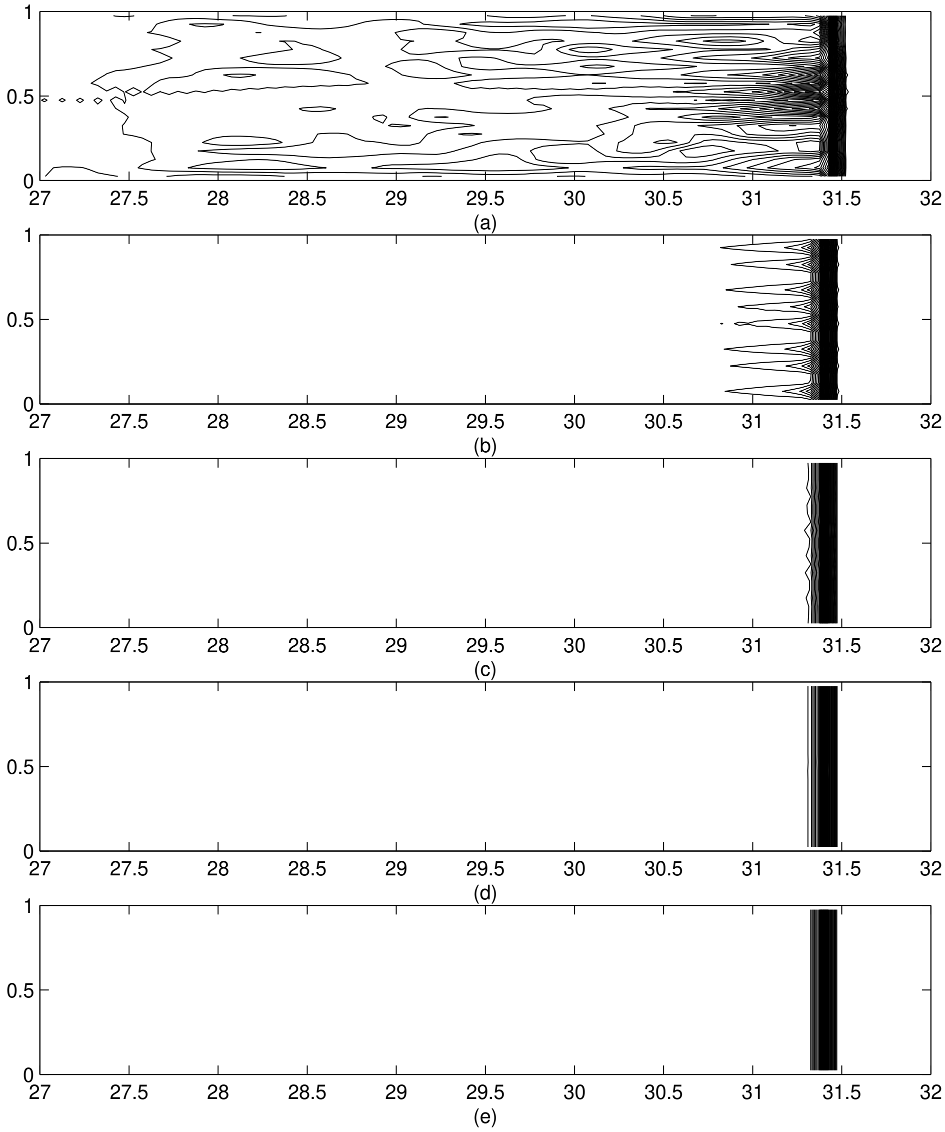

Figure 9: Numerical solutions of the 2D shock tube case, where the location of central line is perturbed odd-evenly. (a)-(d) are from 2nd-order NS Godunov method with (a): $\nu_{phy} = 0.0$, (b): $\nu_{phy} = 0.0005$, (c): $\nu_{phy} = 0.001$ and (d): $\nu_{phy} = 0.0012$. (e) is from 2nd-order van Leer FVS scheme with $\nu_{phy} = 0.0$. As analyzed in this paper, the numerical dissipation in the FVS scheme is $\nu_{num} = \alpha \Delta x$, which is much larger than the physical viscosity in the NS Godunov method.

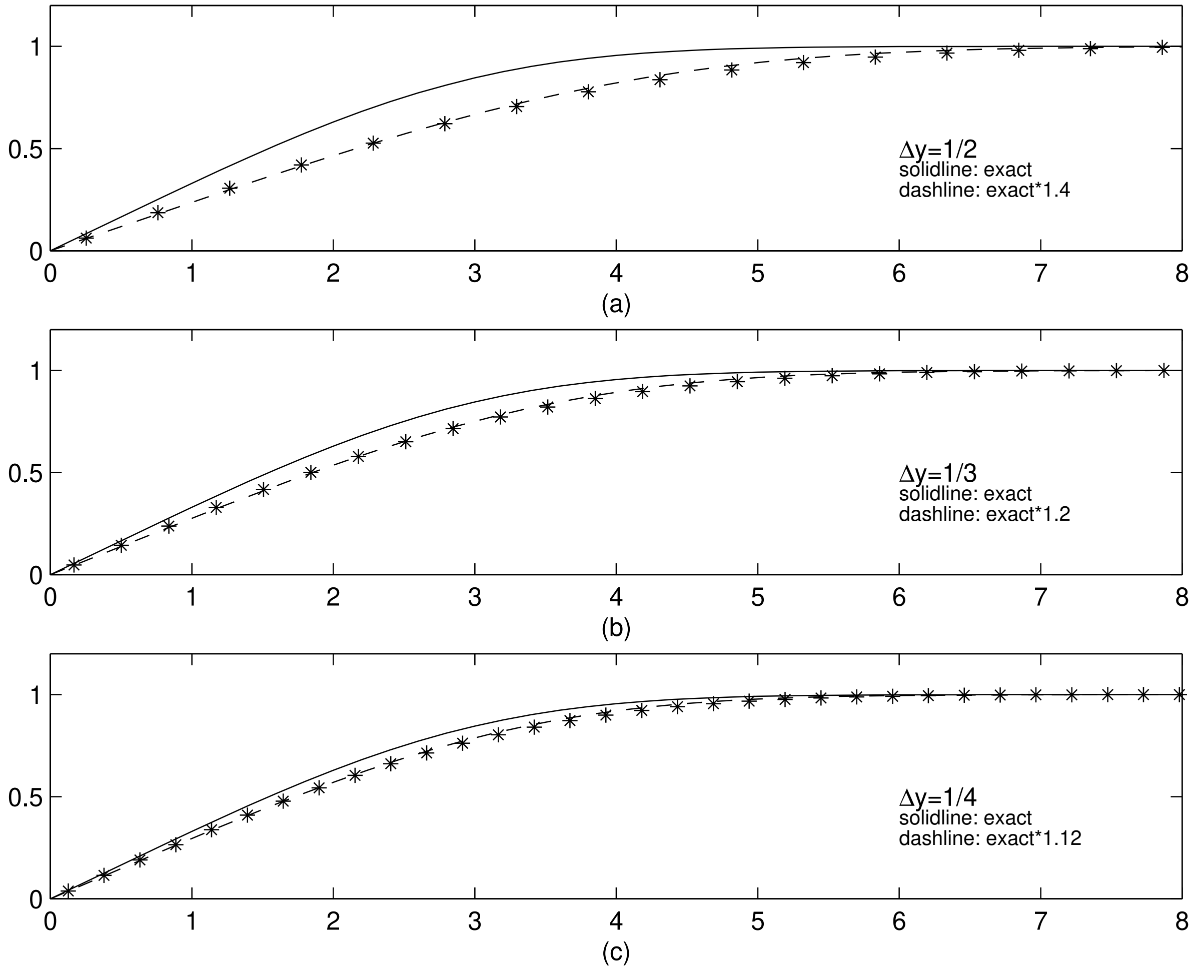

Figure 10: Mesh refinement study of NS van Leer FVS scheme. The dashline is obtained by changing the viscosity in the Blasius solution to fit the numerical data at the outpur location $x = 200.0$. The solid line is the exact Blasius solution obtained from $\nu_{phy} = 0.024$.

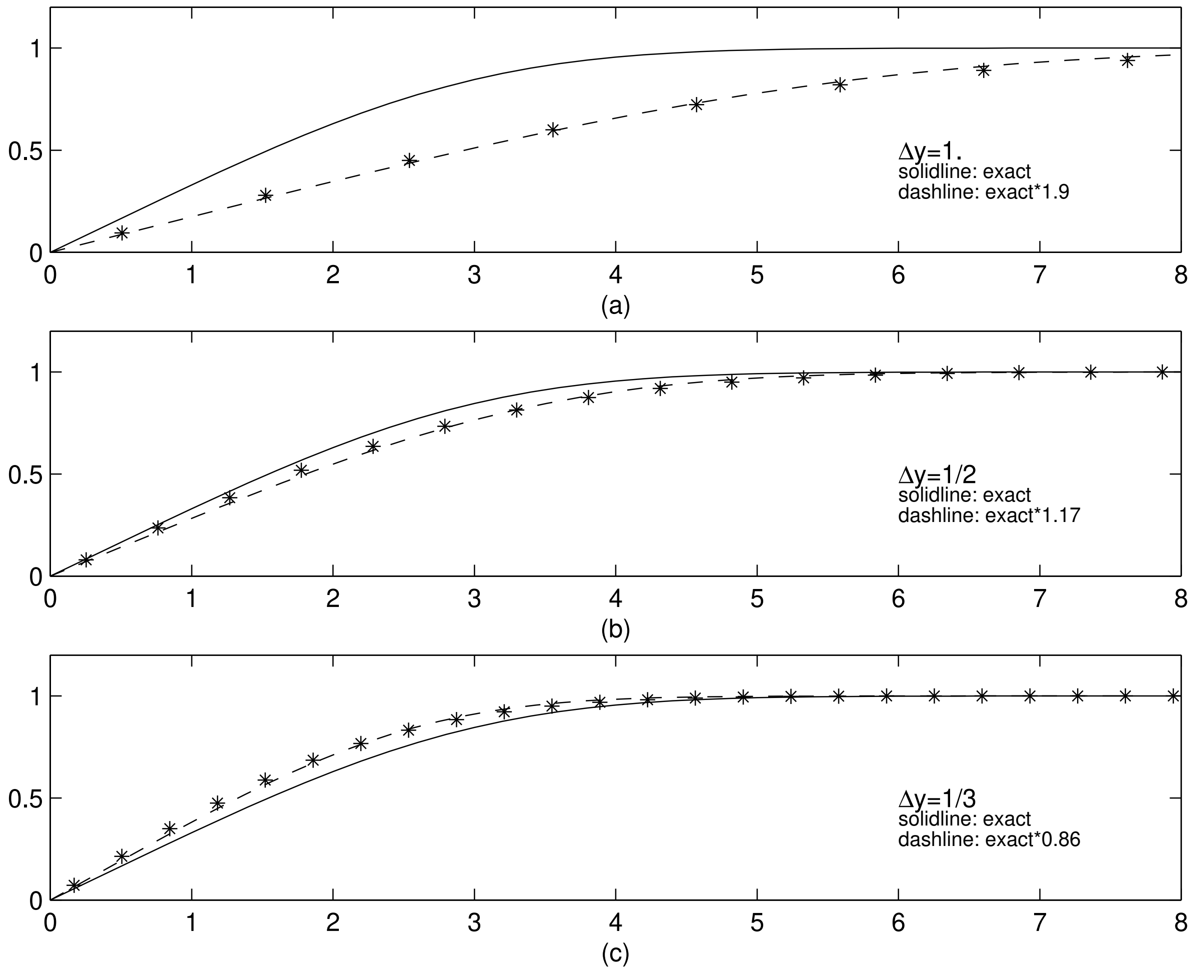

Figure 11: Mesh refinement study of the FVS scheme in the laminar boundary layer case. The van Leer FVS flux function is used directly without including the physical viscous term in the total flux evaluation. The above boundary layer is constructed purely from numerical viscous effect. The dashline is obtained by changing the viscosity coefficient of the Blasius solution to fit the numerical data at the location $x = 200$. The solid line is the exact Blasius solution with $\nu_{phy} = 0.024$.

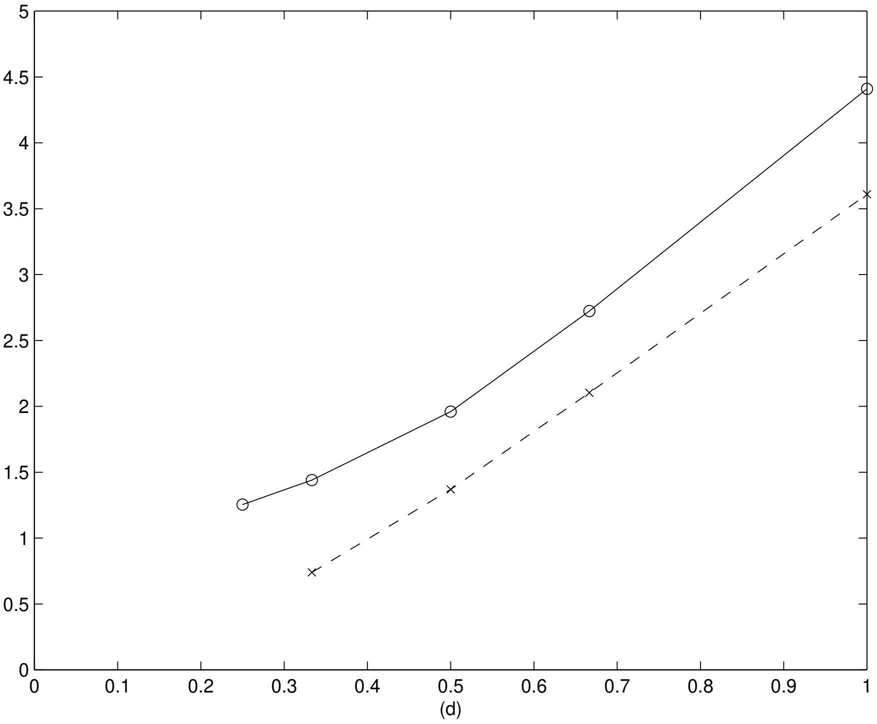

Figure 12: $--\circ--$: plot of $\frac{\nu_{total}}{\nu_{phys}}$ vs. mesh size. $--\times--$: plot of $\frac{\nu_{numer}}{\nu_{phys}}$ vs. mesh size, where $\nu_{phys}$is a constant and equal to 0.024.

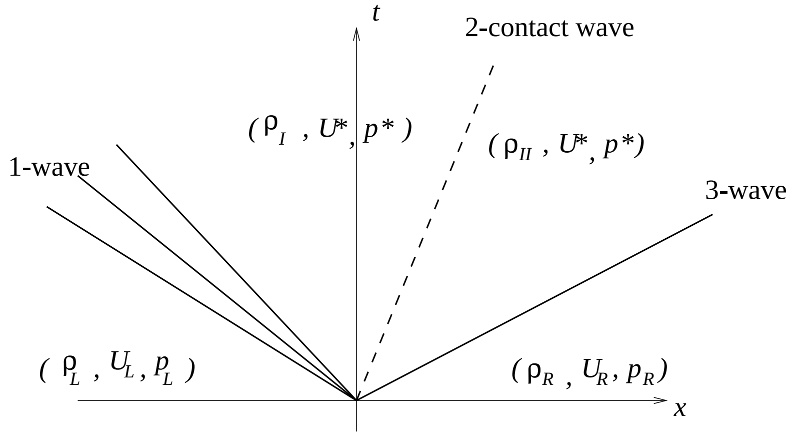

Figure 13: Solution of the Riemann problem in the (x, t)-plane

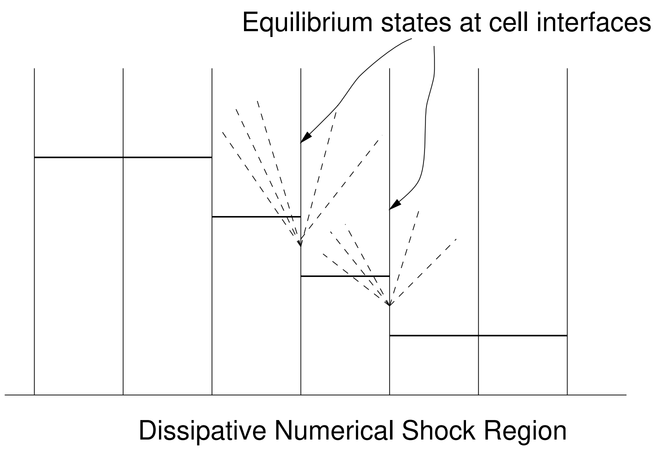

Figure 14: Godunov gas evolution model

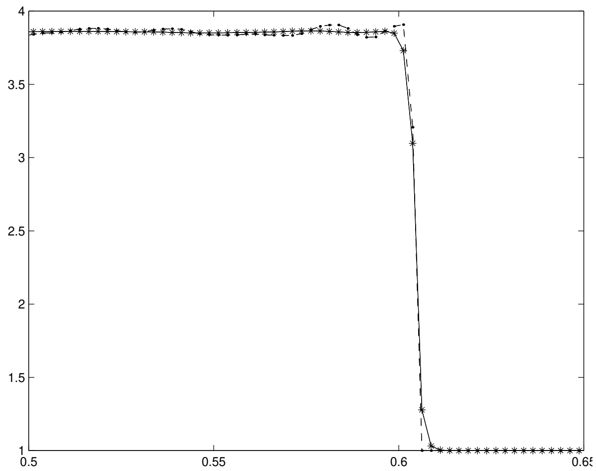

Figure 15: Postshock oscillations of a slowly moving shock. The numerical solutions are from 2nd-order NS Godunov method. $- - - - \cdot - - -$: $\nu = 0.0$, and $- - * - -$: $\nu = 0.001$.

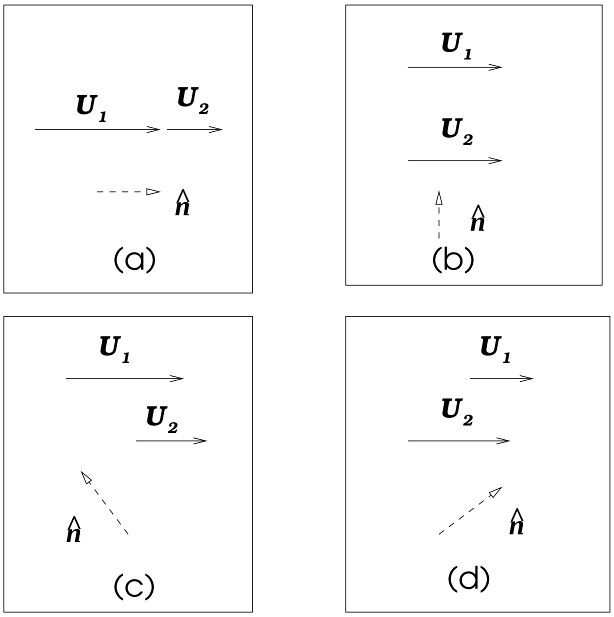

Figure 16: Velocity distributions around a 2-D normal shock looked in different directions, (a): $\hat{x}$, (b): $\hat{y}$, (c): 135°, (d): 45°.

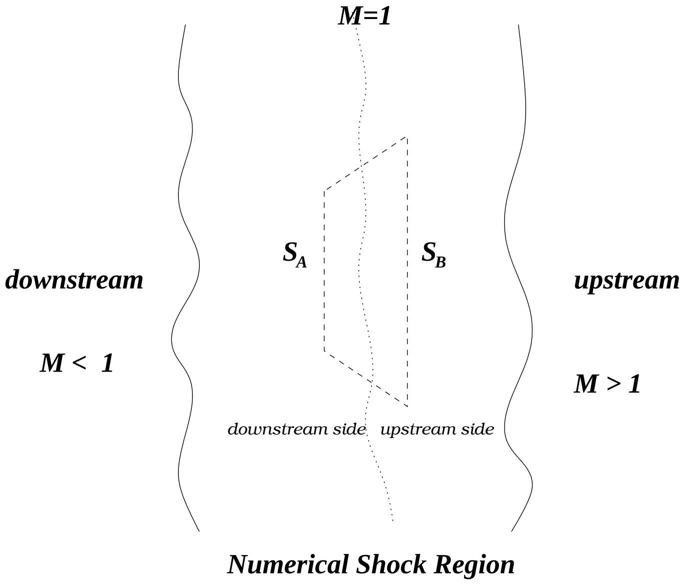

Figure 17: A normal shock in the $\hat{x}$-direction in the 2-D case

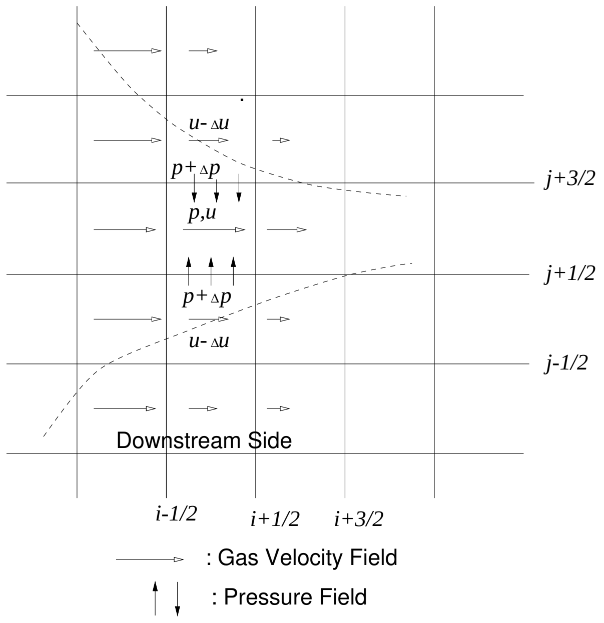

Figure 18: Schematic explanation of shock instability

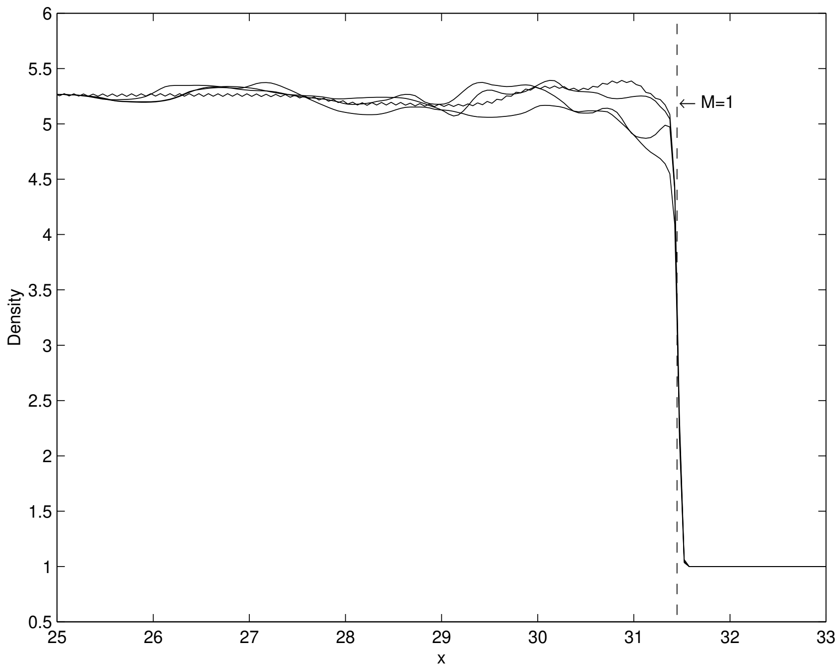

Figure 19: Density distributions of Fig.(9a) along x-direction at different y locations.

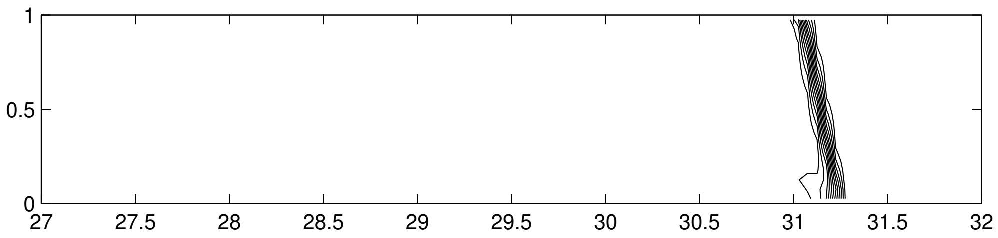

Figure 20: Desity distribution calculated by a 2nd-order Godunov method with $\nu_{phy} = 0.0$. All flow conditions and mesh perturbation are the same as that in Fig.(9a) except the shock front is titled by 10 degree. Shock instability disappears due to the projection dissipations in both directions.